Simulation of the microstructure evolution during the extrusion of two industrial-scale AA6063 profiles

Simulation of the microstructure evolution during the extrusion of two industrial-scale AA6063 profiles.

Marco Negozio[1], Riccardo Pelaccia[2], Lorenzo Donati[1], Barbara Reggiani[2]

[1]DIN Department of Industrial Engineering – University of Bologna,
Viale Risorgimento 2, 40136, Bologna, Italy.
[2]DISMI Department of Sciences and Methods for Engineering, University of Modena and Reggio Emilia,
Via Amendola 2, 42122, Reggio Emilia, Italy.

CORRESPONDING AUTHOR:
Marco Negozio
DIN Department of Industrial Engineering – University of Bologna

Viale Risorgimento 2, 40136, Bologna, Italy.
tel: +39 051 2090 496
e-mail: marco.negozio2@unibo.it

Abstract

The microstructure of lightweight alloys is of a primary interest for manufacturing companies since it affects mechanical strength, crash, corrosion and esthetic properties. Numerical and experimental research activities are needed to investigate the relation between manufacturing process parameters and grain structure evolution in order to control the properties of the final component. In this context, aim of this work is the experimental investigation of the evolution of the microstructure in two different industrial-scale AA6063 aluminum alloy extruded profiles. Furthermore, a novel modeling of the AA6063 recrystallization behaviour is developed and implemented within the commercial FEM code Qform UK Extrusion®. The results of the numerical evaluations are then compared to the experimental data in order to assess the accuracy of the model. A good correlation between numerical predictions and experimental data is found for both profiles, thus proving the reliability of the proposed AA6063 recrystallization model.

Keywords: recrystallization, aluminum alloy, extrusion, fem, microstructure

Introduction

Aluminum alloy profiles are increasingly used for structural application due to their high specific strength, low density, good corrosion resistance and recyclability [1]. In order to produce these profiles, the hot extrusion is the most selected manufacturing process providing mechanical, crash and corrosion properties strictly dependent on the grain size and texture [2-5]. This relation was investigated by several authors [6-8], proving that a finer grain size produces benefits in terms of both mechanical and crash performances. Hence, since microstructure evolves with the extrusion process, it is of industrial and academic interest to investigate the influence of manufacturing parameters on grains size. Moreover, in order to control the final microstructure at a die design stage without performing expensive experimental trial and errors, it is mandatory the development of reliable models for the recrystallization predictions to be implemented in FE (Finite Element) codes.

In Fig. 1 is reported the schematization of the microstructural evolution during the hot extrusion process of aluminum alloys. In more details, Fig. 1a shows the microstructure of the starting billet material, which is fully recrystallized due to the homogenization treatment. Ones the extrusion begins, the dynamic recrystallization (DRX) may occur as consequence of the strain field applied to the material and the high frictional coefficients [8]. This evolution leads to the condition reported in Fig. 1b, where an example of fibrous microstructure is reported. The fibrous grains are marked by a dimension along the extrusion direction several times greater than the width and thickness. After the extrusion, depending on several factors such as the exit temperature, the level of strain applied during extrusion, the chemical composition of the alloy and the quenching conditions (media and time), the static recrystallization (SRX) may also occur [5]. This phenomenon involves the nucleation of new grains and their coarsening, until the older grain structure is replaced. The static recrystallization may be total (Fig. 1c), partial (Fig. 1e) or not occur (Fig. 1d).

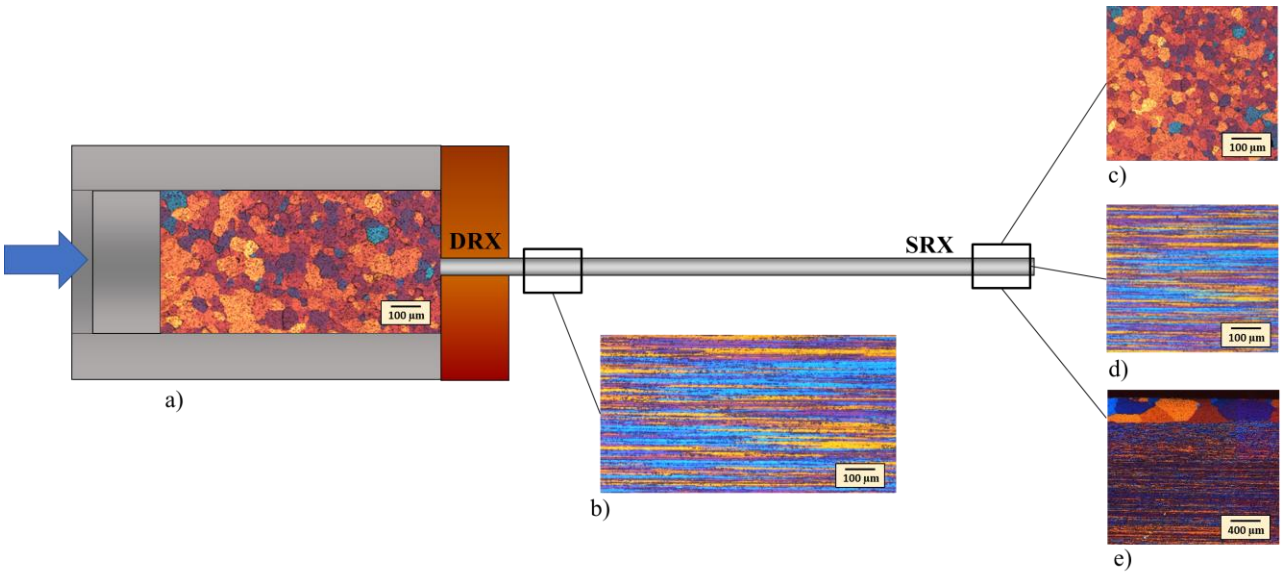

Figure 1: Example of microstructural evolution in the hot extrusion of aluminum alloys: a) microstructure of the billet after homogenization, b) microstructure after extrusion (immediate quenching after the die), c) recrystallized microstructure, d) fibrous microstructure, e) partially recrystallized microstructure.

The dynamic recrystallization behaviour is related to the investigated material and involves nucleation and growth for LSFE (Low Stacking Fault Energy) materials as found in γ-Fe (~-400 mJ/m^2 [9]). Instead, for HSFE (High Stacking Fault Energy) materials as pure aluminum or its alloys (~100-200 mJ/m^2 [10]), DRX involves different mechanisms that are still under investigation from the research community. Focusing on the dynamic recrystallization of aluminum alloys, several

studies were carried out: in 1985, McQueen H.J. et al [11] suggested that original grain, due to the strain field, deforms and, when the thickness becomes of about 2-3 times the subgrain size, it is split into two new grains ("pinch-off"). This theory was called gDRX (Geometric Dynamic Recrystallization) and further investigated in 2004 and 2011 [12-13]. In 2003, Gourdet S. et al. [14] proposed the cDRX (Continuous Dynamic Recrystallization) theory according to which, during deformation, the generation of new grains is related to the evolution of the misorientation angle of subgrains, that increase until LAGB (low angle grain boundaries, which surround the subgrains within the grain) become HAGB (high angle grain boundaries, which surround the grains). In 2008, De Pari L. and Misiolek W. [15] proposed a joint theory jDRX (Joint Dynamic Recrystallization) which combines both gDRX and cDRX algorithms and validate this model on the hot rolling process of a AA6061 aluminum alloy. This theory was further investigated by Donati L. et al. [16] in 2013 in the extrusion of a AA6060 aluminum alloy.

The static recrystallization mechanism, which occurs after the deformation, was analysed by several authors as well. Jonas J.J. et al. [17], Castro-Fernandez F.R. et al. [18], Duan X. and Sheppard T. [19, 20] and Donati L. et al. [14] investigated the formation and evolution of subgrains, which influences the SRX behaviour during the hot extrusion process and, in particular, the relation between the subgrain dimension and the Zener Hollomon parameter [18]. In 1996, Vatne H.E. et al. [21] proposed the modeling of the static recrystallization of aluminum alloys, which depends on the sum of three nucleation contributions: the particle stimulated nucleation, the cube bands nucleation and the grain boundaries nucleation. The modeling of the SRX was also investigated by Sellars C.M. and Zhu Q. [22], in 2000, where the influence of distribution of subgrain size and misorientation between subgrains on the recrystallization nucleation density were analysed. Other authors investigated the static recrystallization modeling: in 2013, Eivani A.R. et al. [23] studied the effect of stored energy and Zener drag pressure on the recrystallization, in 2016 Furu T. et al. [24] simulated the recrystallization behaviour by means of finite element method to predict the grain structure in terms of fraction recrystallized in the extrusion of AA6082 rod profile with different Mn addictions. The modeling of the aluminum alloys recrystallization behaviour in the extrusion of simple geometry profiles (rods) or laboratory-scale extrusions by means of FEM codes was also proposed by Peng Z. and Sheppard T. [25] in 2004, Guzel et al. [26] in 2012, Mahmoodkhani Y. et al. [27] in 2019 and Eivani A.R. et al. [28] in 2020.

In summary, a number of studies and modeling activities were carried out by comparing experimental and numerical data in terms of microstructure evolutions in the hot extrusion of aluminum alloys [16, 25, 29, 30]. However, many of these works were performed using laboratory-scale or simple-profile extrusions as experimental campaigns. None of these models has been extensively tested on extrusions of industrial-scale cases or on complex geometry profiles, thus limiting the strain and strain rate fields for the modeling validation. In addition to that, no combined DRX/SRX simulation of the evolution of grain size after the extrusion process has been proposed.

In this work, two different industrial-scale extrusions of AA6063 aluminum alloy complex profiles were investigated. Numerical activities involving Finite Element (FE) simulations of the two experimental extrusions were performed with the commercial Qform UK® code. Starting from the recrystallization models available in the literature, an innovative one for the DRX/SRX combined prediction have been proposed and validated. A regression approach was suggested for the identification of the AA6063 material constants in order to overcome the limits, uncertainties and consequently errors generated by literature assumptions. An innovative equation for the prediction of the grain boundary area per volume at a given strain was proposed and validated. Finally, a more accurate estimation of the final Zener-Hollomon parameter was realized by the implementation of a

new user-subroutine in the Qform UK code that calculates, in each point of the profile cross-section, the maximum strain rate reached in the deformation path during the material flow. That was necessary because the FEM results of the strain rate values calculated in the profile cross-section (immediately after the bearing zone) are always nearby zero. The experimentally acquired data on grain size were used to calibrate and validate the proposed recrystallization model, comparing the achieved results with the microstructural data for the two industrial-scale profiles. The final aim of this work was to propose a reliable numerical tool able to accurately predict the microstructural behaviour in the hot extrusion of AA6063 aluminum alloy profiles.

Materials and Methods

Two different industrial AA6063 profiles were investigated (Fig. 2) in order to assess the reliability of the recrystallization model. The first solid profile (*a*) was extruded by Indinvest LT plant of Latina (Italy) on an industrial 35 MN press while the second hollow profile (*b*) was produced at Sapa plant in Ornago (MI) on an industrial 30 MN press.

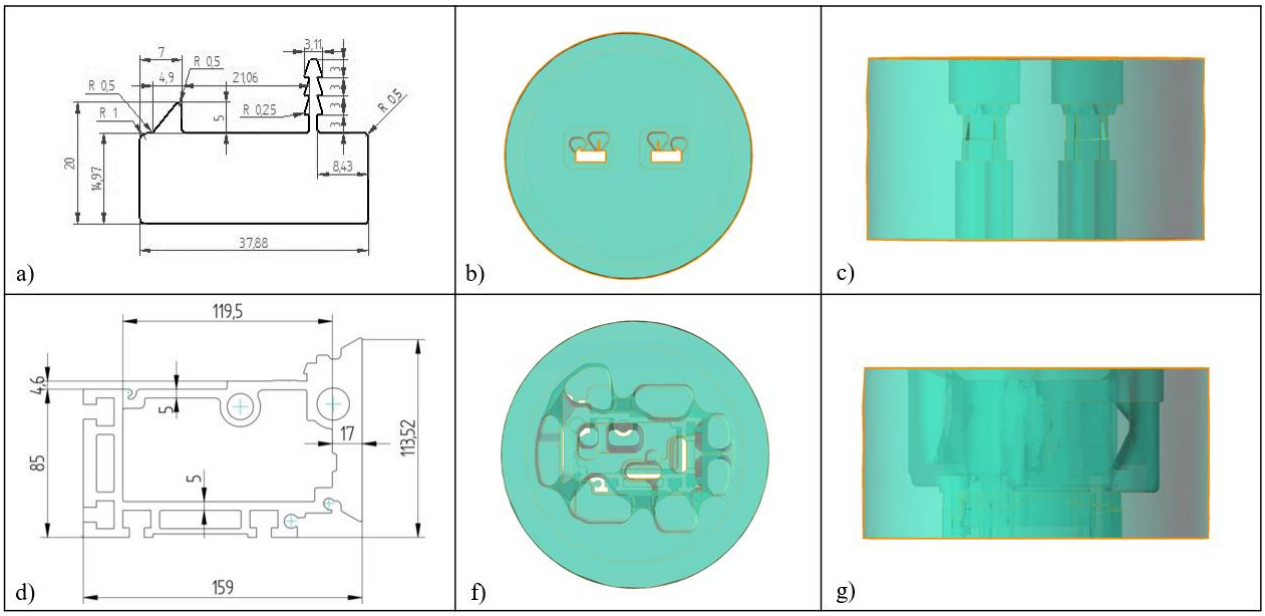

Figure 2: Investigated profiles and die geometries: a) profile *a*, b) top view and c) side view of die for profile *a*, d) profile *b*, f) top view and g) side view of die for profile *b*

In Table 1, the extrusion process and the tool geometry parameters of the two profiles are reported. As shown in Tab. 1 and Fig. 2, the two extrusions reveal different characteristics in terms of temperatures, profile shapes, dimensions and extrusion ratios, thus producing a reliable amount of data for the numerical model calibration and validation. For profile *b*, microstructural data were taken from the work of Gamberoni A. et al. [31], while, for profile *a*, data were experimentally acquired.

The microstructure of profile *a* is shown in Fig. 3 (a-e): the image was acquired by using polarized light microscopy of the samples anodized (40 V dc, 4 min) with Barker's reagent (15 mL HBF_4, 750 mL H_2O). Each measurement of the average grain dimension was carried out according to the ASTM-E112 regulation. The analysed samples were taken at the middle length of the extrusion profile once the process has achieved the thermal steady-state condition. The figure clearly shows a completely recrystallized structure, within an average dimension range from 40 µm (Fig. 3e) to 170 µm (Fig. 3b). In Fig. 3d, an example of PCG (Peripheral Coarse Grain) structure is reported. This structure is characterized by coarse grains with respect to the dimension of the surrounding grains which may reduce crash, mechanical, corrosion and fracture properties.

Table 1: Process parameters and geometry tolerances

Process parameters and geometry tolerances	Profile *a*	Profile *b*
Aluminum alloy	AA6063	AA6063
Extrusion ratio	44	9.6
Ram speed [mm/s]	6.44	8.5
Container temperature [°C]	430	420
Billet temperature [°C]	530	470
Die temperature [°C]	450	450
Ram acceleration time [s]	5	5
Billet length [mm]	670	815
Billet diameter [mm]	254	247
Container diameter [mm]	264	257
Billet Rest length [mm]	15	55

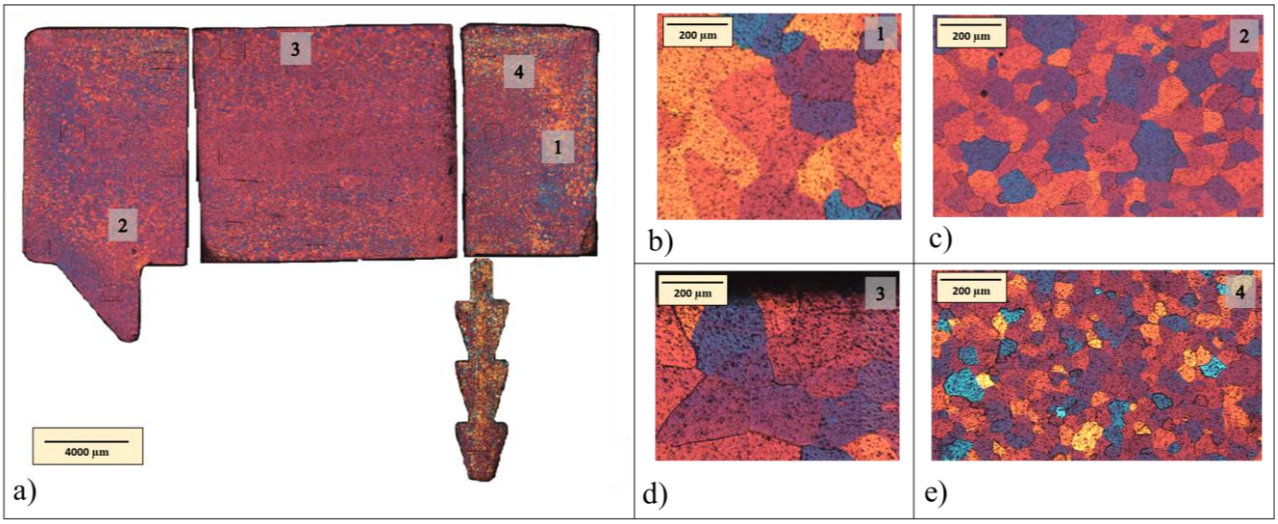

Figure 3: Microstructure of profile *a:* a) overview of the microstructure of the entire profile, b) focus on zone 1, c) focus on zone 2, d) focus on zone 3, e) focus on zone 4

The microstructure of profile *b* is shown in Fig. 4. As for profile *a*, a merge of the different micrographs is reported, revealing a completely recrystallized microstructure, as for profile *a*, within a minimum grain dimension of 55 µm (top-right part of Fig. 1c). The maximum grain dimension (around 500 µm) is detectable where the profile shows PCG, as revealed in Fig. 1e, and AGG (Abnormal Grain Growth) structures, localized in the seam welds (Fig. 1b). Moreover, the microstructure of the profile *b* billet is shown in Fig. 5.

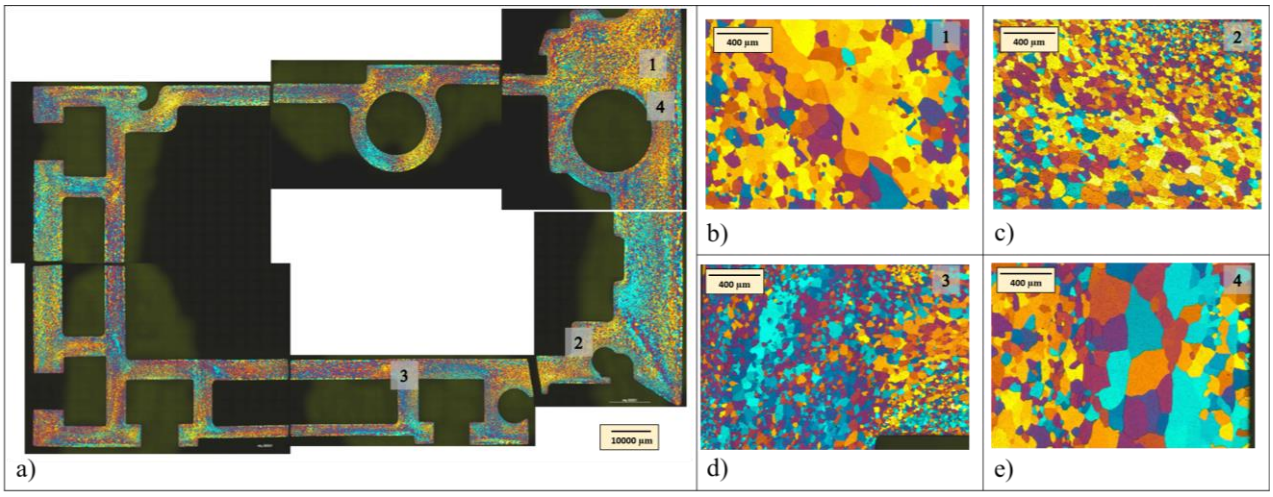

Figure 4: Microstructure of profile *b:* a) overview of the microstructure of the entire profile, b) focus on zone 1, c) focus on zone 2, d) focus on zone 3, e) focus on zone 4.

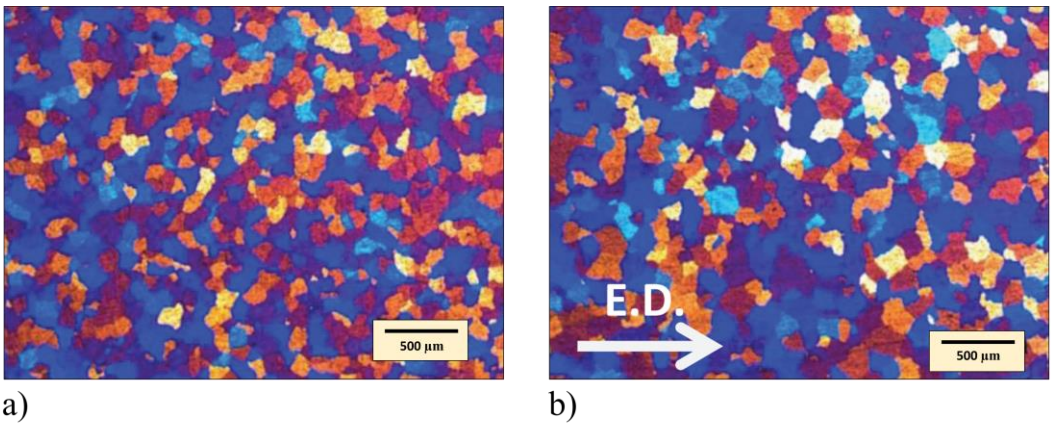

Figure 5: Microstructure of profile *b* billet: a) transversal section of the billet, b) longitudinal section of the billet.

Several grain dimension measurements were performed both for profile *a* and *b*. Part of the data was used to train the material constants of the model for the AA6063 alloy, while another part to validate the achieved results. The procedure is explained in more details in the next section.

Numerical Procedure

Model setup

The modeling of both the dynamic and the static recrystallization mechanisms was carried out. Concerning the dynamic recrystallization, according to the work of Donati L. et al. [16], the average thickness d_t and length d_l of the grains immediately after the bearing zone can be calculated as following:

$$d_t = (d_0 - 2.5 * \delta_{ss}) * (k_1)^{\bar{\varepsilon}} + 2.5 * \delta_{ss} \quad (1)$$

$$d_l = k_2\bar{\varepsilon}^2 - k_3\bar{\varepsilon} + d_0 \qquad \text{if } \varepsilon < \varepsilon_p \quad (2)$$

$$d_l = k_4\bar{\varepsilon}^{-m} + 10\delta_{ss} \qquad \text{if } \varepsilon > \varepsilon_p \quad (3)$$

where ε_p is the critical level of strain for the pinch-off onset, which correspond to a value of 3, δ_{ss} is the subgrain size at the steady-state condition (δ_{ss} = 8.4 μm) and m, k_1, k_2, k_3, k_4 are material constants ($m = 4.75,\ k_1 = 0.4, k_2 = 85.192,\ k_3 = 14.88,\ k_4 = 1.68 * 10^5$ [16]).

Based on a previous work [21], the static recrystallization of a 6XXX aluminum alloy was modelled as:

$$D_{rec} = DN^{-1/3} \tag{4}$$

where D is a material calibration constant and N is the nucleation density. Again, according to [21], the latter was considered as sum of different nucleation components:

$$\mathrm{N} = N_{PSN} + N_{GB} + N_C \tag{5}$$

where N_{PSN} is the nucleation from deformation zones around large particles. N_{PSN} is often the main nucleation mechanism in the commercial alloys which contains large undeformable particles, and involves the growth of nuclei in turbulent deformation zones with random orientations. N_{GB} is the nucleation from old grain boundaries, around which occur deformation zones of randomly oriented subgrains that may act as an additional nucleation site for a random recrystallization texture. N_C is the nucleation from retained cube grains, present in the initial material, which survived the applied deformation. In the following, the selected approach for the evaluation of these nucleation contributions is detailed.

The N_{PSN} was calculated following the equation [21]:

$$N_{PSN} = C_{PSN} \exp\left(\frac{-A_{PSN}}{(Pd - Pz)}\right) \tag{6}$$

where C_{PSN} and A_{PSN} is a material constant, Pd the Stored Energy and Pz the Zener Drag Pressure. The Stored Energy acts as the driving force for recrystallization, in the form of dislocation substructures and concentrations of vacancies [22]. The Zener Drag Pressure, that depend on the alloying elements in solid solution and dispersoids' size and density, retards the recrystallization. Pd was calculated according to [22]:

$$\mathrm{Pd} = \frac{Gb^2}{10}\left[\rho_i(1\text{-}\ln(10b\rho_i^{0,5})) + \frac{2\theta}{b\delta} * \left(1 + \ln\left(\frac{\theta c}{\theta}\right)\right)\right] \tag{7}$$

where G is the material shear modulus (2.05×10^{10} Pa [21]), b the Burgers vector (2.86×10^{-10} m [21]), ρ_i the dislocation density, δ the subgrain size, Θ the misorientation angle and Θc the misorientation angle limit (15°). The dislocation density ρ_i and the misorientation angle Θ evolutions have been taken from [22]. According to this work, ρ_i consists in two parts: the so-called "random" dislocation density and the "geometrically necessary" dislocation density. During plastic deformation, "random" dislocations are created due to work hardening while the "geometrically necessary" dislocation density relates to the lattice curvature. The model for the ρ_i computation proposed in [22] was also investigated in [32], where the dependency of dislocation density and misorientation angle with the strain rate $\dot{\varepsilon}$, the temperature T and the strain ε was reported. Fig. 6a and Fig. 6b shows this dependence of the two investigated parameters.

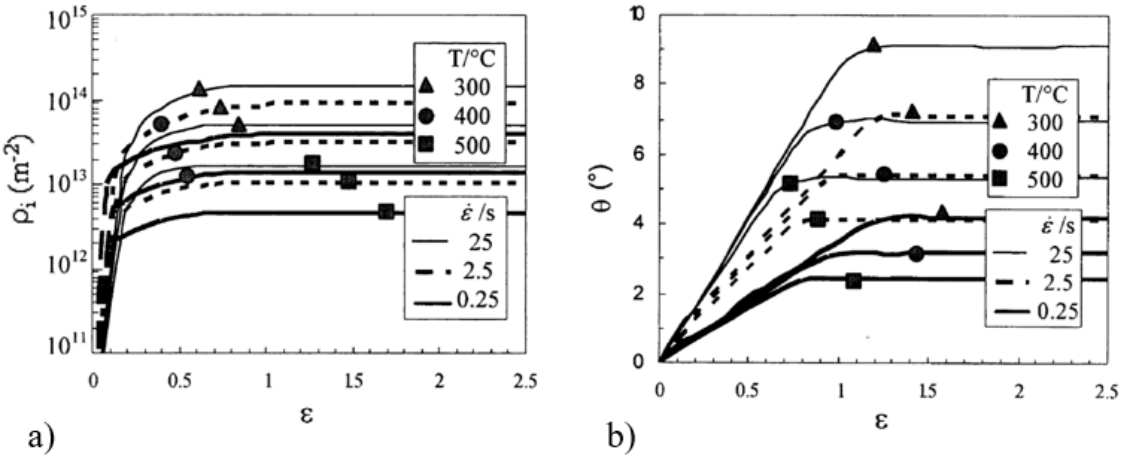

Figure 6: a) Dislocation density [32], b) Misorientation angle [32].

The subgrain and the Zener-Hollomon parameters were calculated according to [16]:

$$\frac{1}{\delta} = C\ (lnZ)^n \tag{8}$$

$$Z = \ \dot{\varepsilon}\ exp\ \left(\frac{Q}{RT}\right) \tag{9}$$

where C=3.36x10^{-9} m^{-1}, n=5.577, Q is the activation energy of the AA6063 (232350 J/mol*K [33]), $\dot{\varepsilon}$ is the maximum strain rate for each point of material flow during the extrusion deformation path and R is the universal gas constant (8.341 J/mol).

The Zener Drag pressure depends on the dispersoids and alloying elements in solid solution and act in opposition to the static recrystallization [34]. It can be expressed as follow:

$$Pz = \frac{3 * f * \gamma}{4 * r} \tag{10}$$

where f and r are the fraction area and the mean size of the dispersoids, respectively, and γ is the grain boundary energy (0.3 $\frac{J}{m^2}$ [35]). In this work, values for f and r were taken from [36], where an experimental study was made to characterize the density and spatial distribution of dispersoids in Al-Mg-Si alloys. In the AA6063 aluminum alloys, since the content of Mn, Cr or Zr is below 0.1 wt%, there are a low amount of dispersoids and, consequently, the retarding force for the recrystallization is very low. Different 6XXX where analysed and it results that an average value of 0.023% was found for the fraction area and around 60 nm for the mean size of the AA6063 dispersoids.

The second contribution to the nucleation density N_{GB} was modeled according to [21]:

$$N_{GB} = \ C_{GB}\ \delta\ A(\varepsilon)\ S_{GB} \tag{11}$$

where C_{GB} is a material constant, δ the subgrain size, $A(\varepsilon)$ the grain boundary area per volume at a given strain and S_{GB} the number of subgrain larger than a critical subgrain size δ^*, calculated as followed:

$$\delta^* = \frac{4\ \gamma}{Pd - Pz} \tag{12}$$

According to what reported in literature [21], $A(\varepsilon)$ was modeled as:

$$A(\varepsilon) = \frac{1}{D_0}[(\exp(\varepsilon) + \exp(-\varepsilon) + 1)] \quad (13)$$

The third contribution to the nucleation density N_C was modeled according to [21]:

$$N_C = C_C\, \delta\, A(\varepsilon)\, S_C \quad (14)$$

where C_C is a material constant and S_C the number of subgrains larger than a critical subgrain size δ^* within the cube grains. As acceptable approximation, it can be assumed S_C=S_{GB}=S [21].

Numerical Investigation

The numerical modeling of the extrusions was performed using the Arbitrarian Lagrangian Eulerian FEM code Qform Extrusion®. The constitutive model used for the description of plastic AA6063 aluminum alloy flow stress was proposed by Hensel-Spittel [37]: according to the equation, flow stress $\bar{\sigma}$ depends on the contribution of strain $\bar{\varepsilon}$, strain rate $\dot{\bar{\varepsilon}}$ and temperature T:

$$\bar{\sigma} = A \cdot e^{m_1 T} \cdot \bar{\varepsilon}^{-m_2} \cdot \dot{\bar{\varepsilon}}^{-m_3} \cdot e^{\frac{m_4}{\bar{\varepsilon}}} \cdot (1+\bar{\varepsilon})^{m_5 T} \cdot e^{m_7 \bar{\varepsilon}} \cdot \dot{\bar{\varepsilon}}^{m_8 T} \cdot T^{m_9} \quad (15)$$

The values of the Hensel-Spittel constants (m1-m9) and material properties are reported in Tab. 2 and Tab. 3.

Table 2: Hensel-Spittel and for the AA6063 aluminum alloy [38].

Parameters	AA6063
A	1014.7 [MPa]
m1	-0.00438 [K^{-1}]
m2	0.2425
m3	-0.0965
m4	-0.000438
m5	-0.000766 [K^{-1}]
m7	0.002939
m8	0.000291 [K^{-1}]
m9	0

Table 3: Material parameters for the AA6063 aluminum alloy

Material Properties	AA6063
Density [Kg/m3]	2690
Specific heat [J/kg K]	900
Thermal conductivity [W/m K]	200
Thermal expansivity [m/K]	2.34*10-5
Young's modulus [GPa]	68.9
Poisson's ratio	0.33

The friction conditions between workpiece and tools during the manufacturing process were set according to the default values optimized for extrusion in the Qform database (Tab. 4).

Table 4: Friction conditions.

Surface	Friction condition
Billet-Container	Sticking condition
Billet-Ram	Sticking condition
Billet-Die	Sticking condition
Bearings	Levanov model (m = 0.3, n = 1.25)

In order to validate the simulations of the extrusion processes, the numerical values of profile temperature and extrusion load were compared to the ones acquired during the experimental tests. In Fig. 7, these comparisons are reported for profile *b*: a maximum extrusion load of 26.5 MPa (Fig. 7a) was found numerically, while 26 MPa (Fig. 7b) was the value acquired from the press. About the profile temperature, the experimentally acquired value was 542 °C (Fig. 7d) while the numerical was 539 °C (Fig. 7c). This value was taken from the point in which the pyrometer was applied. A similar accuracy was found for the simulation of profile *a*.

The computational time of the FEM simulation of the extrusion processes were 28 hours for profile *a* and 46 hours for profile *b*.

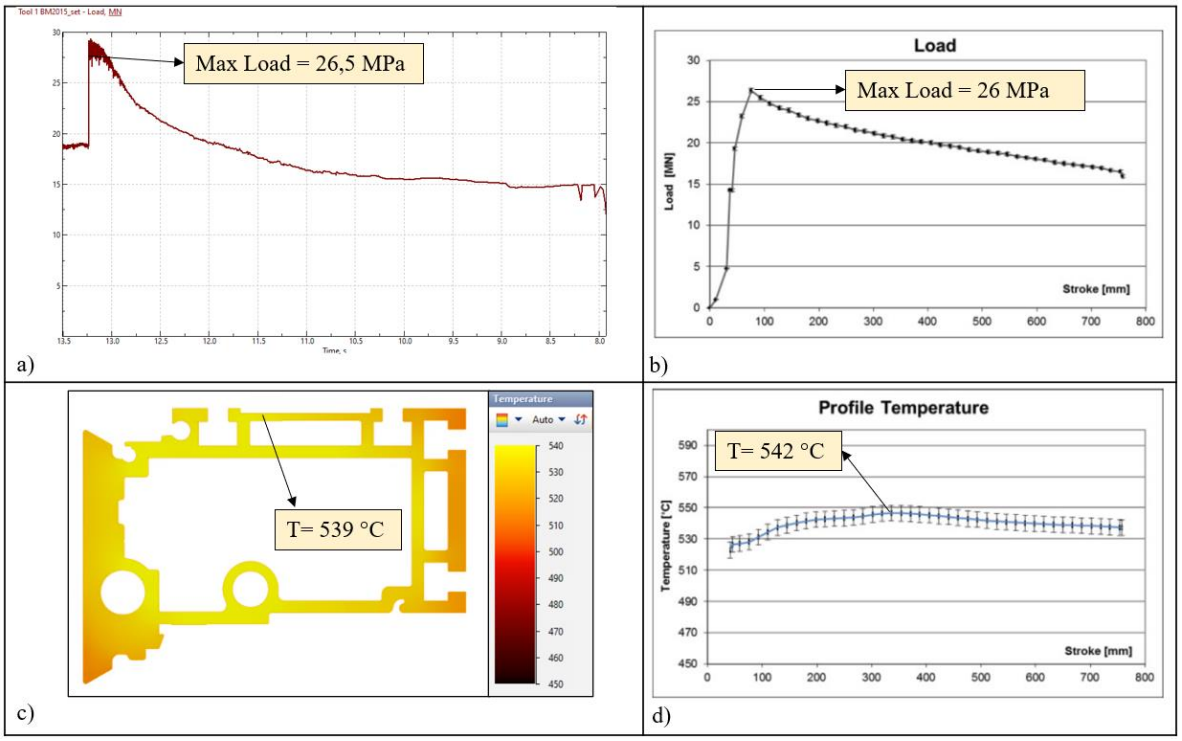

Figure 7: Profile *b*: a) numerical extrusion load, b) experimental extrusion load, c) numerical profile temperature, d) experimental profile temperature.

Results and Discussion

In order to obtain the material constants of the recrystallization model and to predict the AA6063 recrystallization behaviour, the Levenberg-Marquardt non-linear regression algorithm [39], implemented in Matlab®, was applied using as input data a number of values of grain size

experimentally calculated in a total of 100 points, 50 of profile *a* and 50 for profile *b*, and, for each considered point, the values of temperature, strain and strain rate calculated by the FEM simulation using Qform software. The points used for the optimization were taken from the "calibration set" of points. A different set of points ("validation set") were used to validate the results of the numerical microstructure prediction.

Considering the trend of eq. 13, since this equation was investigated in rolling processes which typically have stain values considerably lower than 10 [21], it has been noticed that for values of strain higher than 10 (Fig. 8a), typical of industrial-scale extrusions, the formula returned

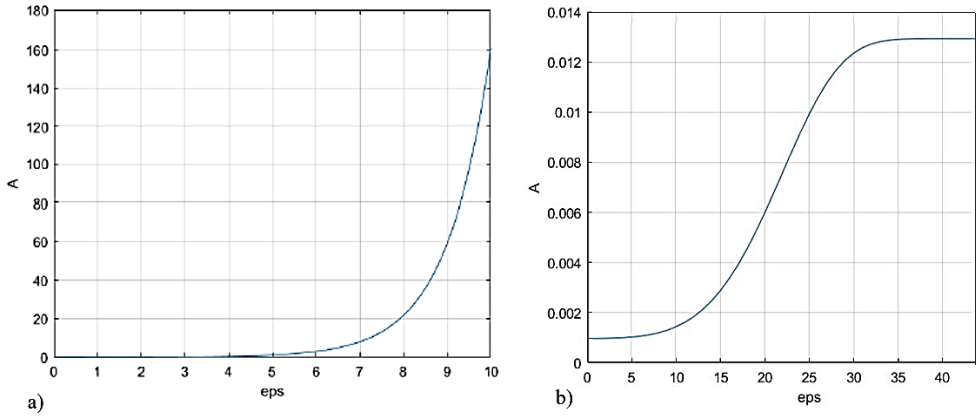

Figure 8: a) A(ε) calculated according to Eq. (13), b) schematic behaviour of A(ε) calculated according to Eq. (16)

unreasonably high values of $A(\varepsilon)$ and, consequently, of N_{GB} and N. For this reason, $A(\varepsilon)$ has been calculated according to eq. 16, limiting the growth of the parameter to a maximum value (Fig. 8b):

$$A(\varepsilon) = \frac{1}{D_0}\left[p_1 - p_2\, e^{p_3\, \varepsilon^{p_4}}\right] \tag{16}$$

where p_1, p_2, p_3, p_4 are material constants. These values were added to the other material constants and optimized using the Levenberg-Marquardt algorithm mentioned above.

The outputs of the non-linear regression method are summarized in Tab. 5. Once obtained these values, the model was implemented into Qform extrusion and used to calculate the grain size dimension of both extruded profiles, using as input values the results of the FEM simulation of the extrusion process in terms of temperature, strain and strain rate.

Table 5: Recrystallization model material constants AA6063

Material constants	AA6063
C_{PSN}	4.99962 e^{13}
A_{PSN}	864686
C_{GB}	0.0022045
C_C	0.0022045
p_1	1.9
p_2	1.06
p_3	1 e^{-7}
p_4	6

In Fig. 9, the results of the dynamic recrystallization predictions were reported. These simulations report the grain size of the profile immediately after the die, where static recrystallization still not occurred. Since both profiles presented a completely recrystallized microstructure, there were no experimental image of the fibrous grain for the validation of the DRX predictions.

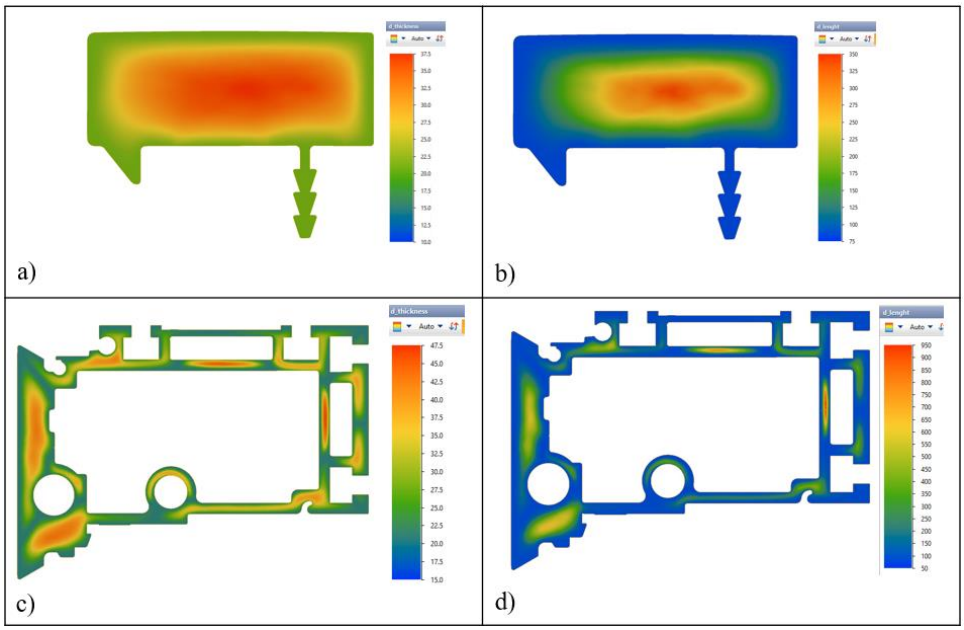

Figure 9: a) Profile *a*, DRX numerical grain thickness, b) Profile *a*, DRX numerical grain length, c) Profile *b*, DRX numerical grain thickness, b) Profile *b*, DRX numerical grain length

In Fig. 10, the numerical predictions of the grain size after the static recrystallization are reported for both profiles. Red and blue areas correspond to the part of the profile in which the grain size have higher and lower dimensions, respectively. The numerical range of grain size dimension resulted between 44 µm and 148 µm for profile *a* (Fig. 10a) and between 32 µm and 396 µm for profile *b* (Fig. 10b).

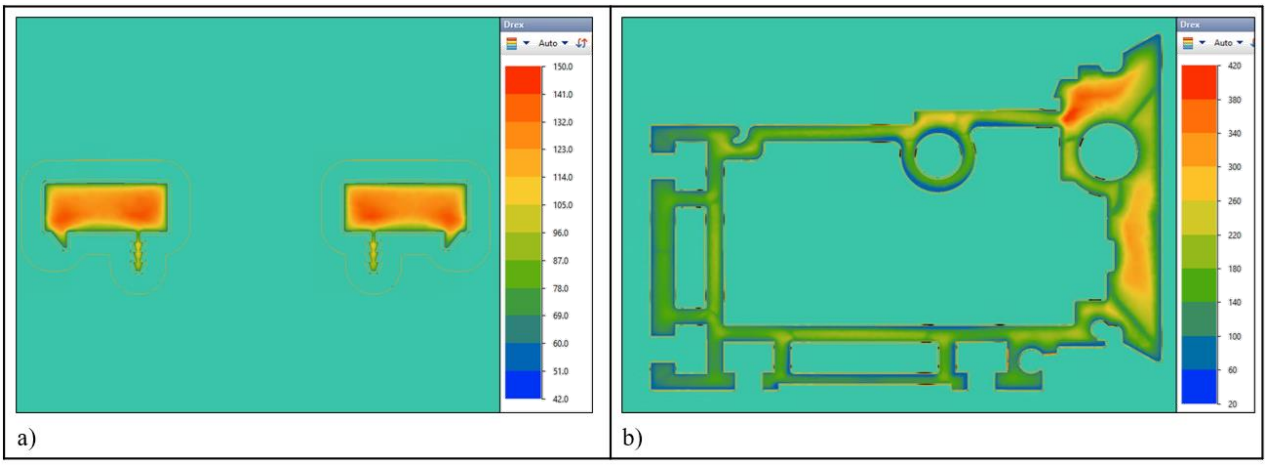

Figure 10: a) Numerical recrystallized grain size of profile *a* [µm], b) Numerical recrystallized grain size of profile *b* [µm].

In Fig. 11, the experimental-numerical microstructure comparison for profile *a* is reported: the red areas of Fig. 11b represent the points where the predicted grain size has higher dimension while the green/blu areas the lower dimension. As clearly visible by comparing Fig. 11b with Fig. 11c-f, a good matching between zones with coarse and smaller grains was found. Since the PCG recrystallization

behaviour is not modeled within the algorithm, the prediction of the grain size where PCG occurred, as in the top surface of Fig. 11d, is not accurate.

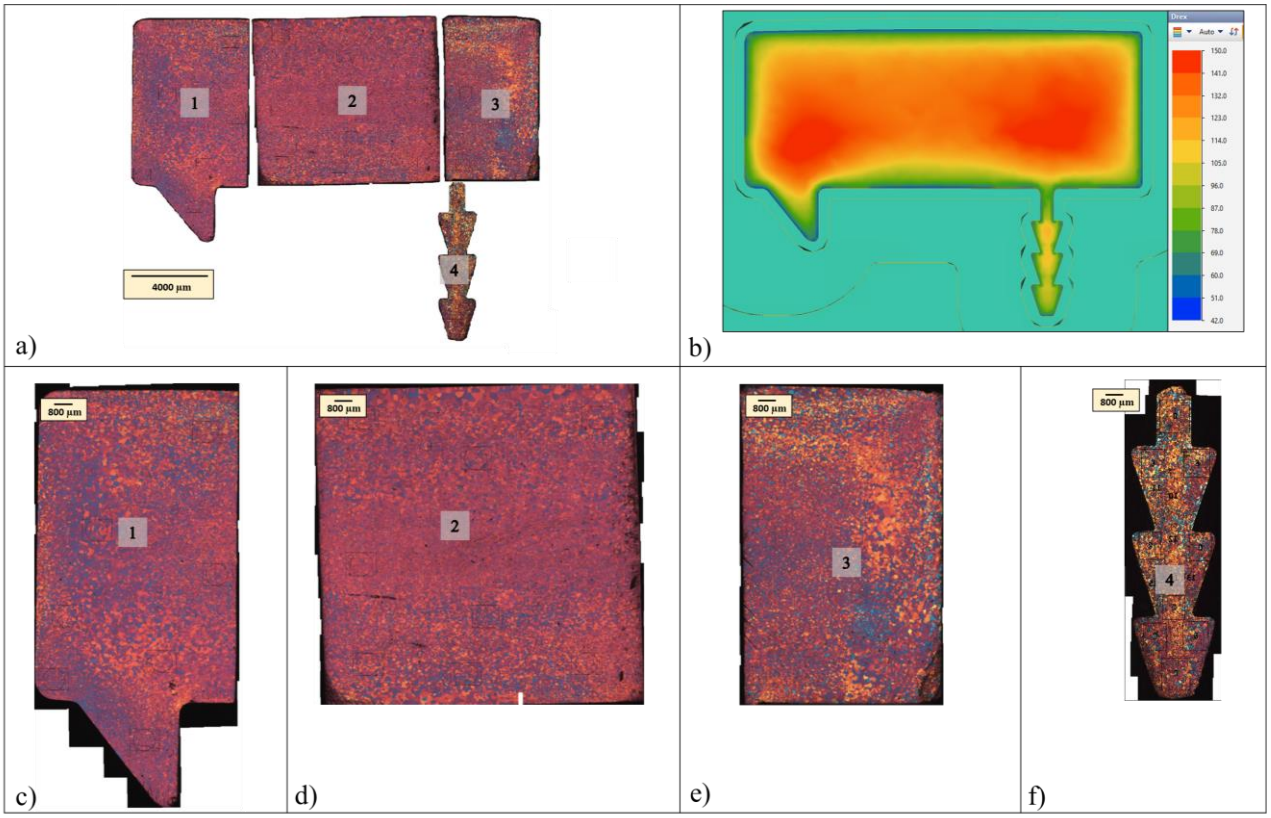

Figure 11: Comparison between experimental and numerical grain size of profile *a*: a) experimental, b) numerical, c) focus on zone 1, d) focus on zone 2, e) focus on zone 3, f) focus on zone 4.

In Fig. 12, the experimental- numerical comparison of the grain size for profile *b* is reported. As for the profile *a*, the predictions match the general trend of grain size. For example, zone 1 and 2 of Fig. 12c, which show higher grain dimensions, correspond to the areas in red with higher grain size prediction. Moreover, the numerical procedure was able to catch the bigger grains in the massive zone of the profile nearby the round hole (Figs. 12c-d) rather than in the thinner section (Figs. 12e-f). As for profile *a*, the prediction where PCG and AGG occurred is not accurate (zone 3 and 4 in Fig. 12c) since the model does not consider these phenomena.

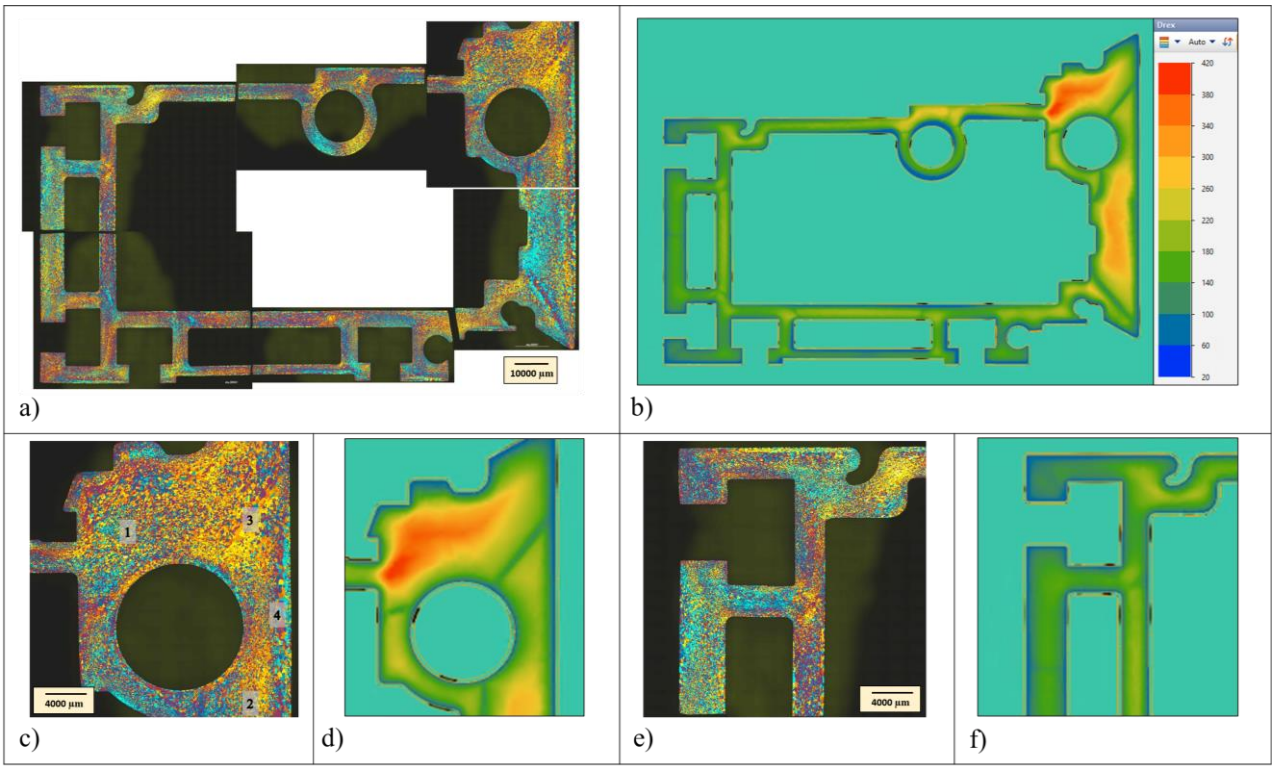

Figure 12: a), c), e) Experimental and b), d), f) numerical grain size of profile *b*.

After the visual examination, a quantitative analysis was carried out. A considerable number of points (taken randomly from the profiles area) were investigated for both profiles by returning the difference between the rain size dimension as experimentally collected and numerically predicted.

In Fig. 13, the measurements made for profile *a* are shown. In details, the x-axis represents the diameter of grains experimentally measured while the y-axis represents the numerical predicted dimensions. Consequently, if the numerical measure perfectly matches the experimental one, the point is expected to be exactly on the 45° orange line. The more the numerical prediction deviates from the real values, the more the red dot deviates from the orange line. In order to facilitate the understanding of the prediction accuracy, two additional green lines were reported that correspond to a ± 25% of error. Since the high number of both process and metallurgical factors affecting the final grain size, the industrial complexity of the analysed extruded geometries and the approximations deriving from the selected measurement methodology for the experimental analysis of the grain dimension, the range of ± 25% of error, also used by Donati L. et al. in [16] for the analysis of a laboratory-scale extruded profile, should be considered as a range of excellent prediction accuracy.

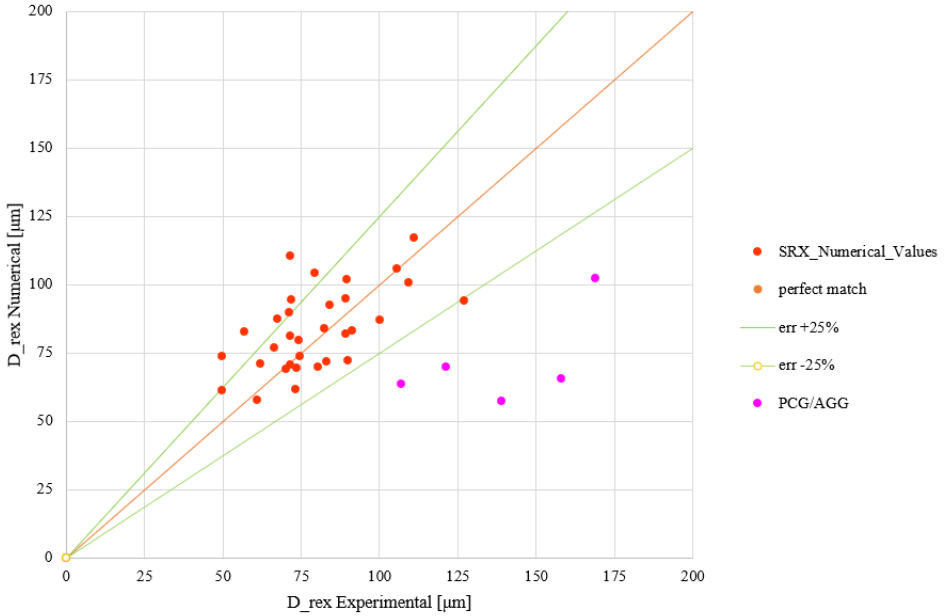

Figure 13: Comparison between experimental and numerical grain size of profile *a.*

As can be seen, the major part (70%) of the red dots fall within the green lines, thus indicating the accuracy and reliability of the developed recrystallization model. If PCG/AGG areas are not considered, the error of the predictions was always below the 35%. Some purple points are significantly below the -25% error line, suggesting an underestimation of the grain size, since extracted from PCG and AGG zones.

In Fig. 14, the same analysis were carried out for profile *b*. In this case, the error of over the 60% of the measurements remains between +25% and -25%. The purple points where the error result significantly high are all taken from PCG/AGG zones. If PCG/AGG areas are not considered, the error of the predictions was always below the 30%.

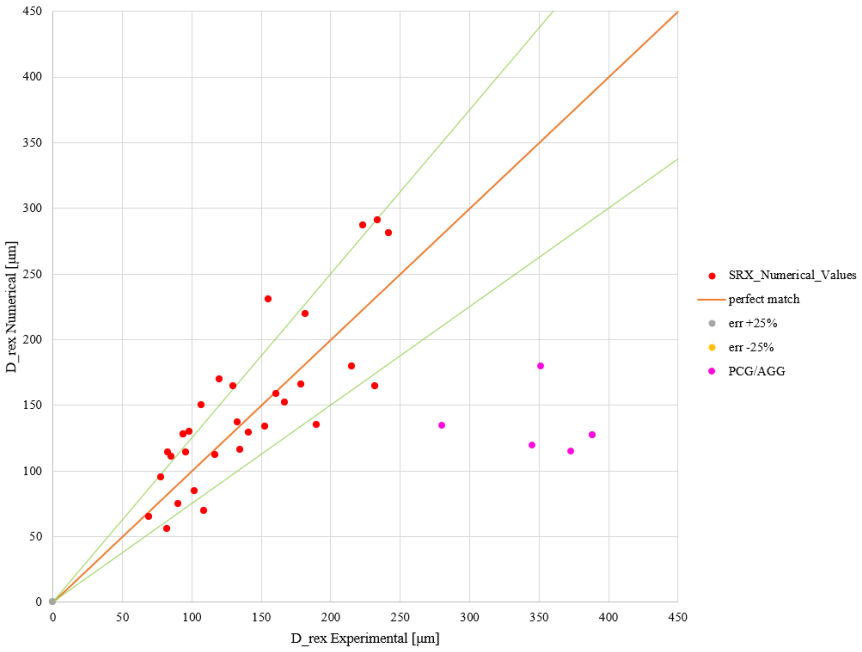

Figure 14: Comparison between experimental and numerical grain size of profile *b.*

Conclusions

In the present work, the development of the recrystallization model of the AA6063 aluminum alloy was carried out together with the FEM simulation of two industrial-scale extrusions using Qform Extrusion FEM code. The microstructural analysis of the two profiles were performed and the collected data were used for the validation of the proposed model. The main outcomes of this work can be summarized as following:

- The results of the extensive experimental analysis on the recrystallization of a AA6063 aluminum alloy were collected and discussed: the microstructures of the Hydro profile were used for the calibration of the model while the microstructures of Profile a and b for the model validation.
- An innovative DRX/SRX combined recrystallization model was developed and optimized for the prediction in AA6063 aluminum alloys. A regression approach was proposed to identify AA6063 material constants. An innovative equation for the prediction of the grain boundary area per volume at a given strain was suggested and validated. Finally, a more reliable estimation of the Zener-Hollomon parameter was realized through the calculation of the maximum strain rate reached in the deformation path during the material flow in each point of the profile cross-section.
- FEM simulation of the analysed extrusion processes were carried out with an average error in the extrusion load and temperature prediction below the 2%, thus proving the reliability of the simulations. The good accuracy combined with the relatively low computational time of the two FEM simulations (28 hours for profile *a* and 46 hours for profile *b*) have shown the usefulness that this tool may have for extruder and die makers.
- A good experimental-numerical agreement was achieved in terms of grain size dimensions. For profile a, if PCG and AGG areas are not considered, the error of the prediction was in the 100% of the measurements below the 35%. If PCG and AGG areas are considered in the evaluation, the error of over the 70% of the points remained below the 25%. For profile b, if PCG and AGG areas are not considered, the error of the predictions was in the 100% of the measurements below the 30%. Considering PCG and AGG areas, error of over the 60% of the points remained below the 25%. The accuracy of the prediction was similar to previous work where simple geometries or laboratory-scale extruded profiles were analysed [16, 29].
- Future developments of this work include the validation of the proposed model over additional experimental cases and the improvement of the grain size prediction in AGG/PCG areas.

Acknowledgements: the authors would like to thank Almax Mori (Italy) and Mr. Tommaso Pinter for providing the extruded profile *a* for the microstructural analysis.

Declarations':

Funding:

Conflicts of interest/Competing interests: Authors do not have a financial relationship with the organization that sponsored the research. They should also have full control of all primary data and agree to allow the journal to review their data, if requested.

Availability of data and material: Not applicable

Code availability:

Authors' contributions: Not applicable

References

1. Sun HT, Wang J, Shen GZ, Hu P. Application of warm forming aluminum alloy parts for automotive body based on impact. International Journal of Automotive Technology 2013;14;605–610. https://doi.org/10.1007/s12239-013-0065-4.
2. Fan XH, Tang D, Fang WL, Li DY, Peng YH. Microstructure development and texture evolution of aluminum multi-port extrusion tube during the porthole die extrusion. Materials Characterization 2016;118;468-480. https://doi.org/10.1016/j.matchar.2016.06.025.
3. Rivas A, Muñoz P, Camero S, Quintero O. Effect of the microstructure on the mechanical properties and surface finish of an extruded aa-6063 aluminum alloy. Advanced Materials Science and Technology. 1999;1;15-23.
4. Arnoldt AR, Schiffl A, Höppel HW, Österreicher JA. Influence of different homogenization heat treatments on the microstructure and hot flow stress of the aluminum alloy AA6082. Materials Characterization 2022;191;112-129. https://doi.org/10.1016/j.matchar.2022.112129.
5. Sheppard T. Prediction of structure during shaped extrusion and subsequent static recrystallisation during the solution soaking operation. Journal of Materials Processing Technology 2006;177;26–35. https://doi.org/10.1016/j.jmatprotec.2006.04.099
6. Parson N, Fourmann, J, Beland JF, Aluminum Extrusions for Automotive Crash Applications. SAE Technical Papers 2017;1–16. https://doi.org/10.4271/2017-01-1272.
7. Wu T, Ding XF, Sun J, Zhang WD, Sun DB, Wang LC. Effects of the Aging Time and Temperature on the Microstructures and Mechanical Properties of 6082 Aluminum Alloy Extrusions. Advanced Materials Research 2013;652–654;1035–1042. https://doi.org/10.4028/www.scientific.net/amr.652-654.1035.
8. Bandar AR, Claves SR, Lu J, Matous K, Misiolek WZ, Maniatty AM. Microstructural Evaluation of 6xxx Aluminum Alloys for Computer-Simulated Texture Prediction. Proceedings of the Aluminum Extrusion Technology Seminar, ET 2004, Orlando, FL, 2004;1;169-176.
9. Niessen F, Li W, Werner KV, Lu S, Vitos L, Villa M, Somers MAJ. Ab initio study of the effect of interstitial alloying on the intrinsic stacking fault energy of paramagnetic γ-Fe and austenitic stainless steel, Acta Materialia 2023;253:118967. https://doi.org/10.1016/j.actamat.2023.118967.
10. Muzyk M, Pakiela Z, Kurzydlowski KJ. Ab initio calculations of the generalized stacking fault energy in aluminium alloys, Scripta Materialia 2011;64(9):916-918. https://doi.org/10.1016/j.scriptamat.2011.01.034.
11. McQueen HJ, Knustad O, Ryum N, Solberg JK. Microstructural evolution in Al deformed to strains of 60 at 400°C. Scripta Metallurgica 1985;19(1);73-78. https://doi.org/10.1016/0036-9748(85)90268-6.
12. McQueen HJ, Kassner ME. Comments on 'a model of continuous dynamic recrystallization' proposed for aluminum. Scripta Materialia 2004;51(5);461–465. https://doi.org/10.1016/j.scriptamat.2004.05.027.
13. McQueen HJ, Spigarelli S, Kassner ME, Evangelista E. Hot Deformation and Processing of Aluminum Alloys, CRC Press, Taylor and Francis Group, Boca Raton FL, USA: 2011.
14. Gourdet S, Montheillet F. A model of continuous dynamic recrystallization. Acta Materialia 2003;51(9);2685–2699. https://doi.org/10.1016/S1359-6454(03)00078-8.
15. De Pari L, Misiolek W. Theoretical predictions and experimental verification of surface, grain structure evolution for AA6061 during hot rolling. Acta Materialia 2008;56;6174–6185. https://doi.org/10.1016/j.actamat.2008.08.050.
16. Donati L, Segatori A, El Mehtedi M, Tomesani L. Grain evolution analysis and experimental validation in the extrusion of 6XXX alloys by use of a lagrangian FE code. International Journal of Plasticity 2013;4670-81. https://doi.org/10.1016/j.ijplas.2012.11.008.
17. Jonas JJ, Sellars CM, McGregor Tegart WJ. Strength and structure under hot-working conditions. Metallurgical Reviews 1969;14;1–24. https://doi.org/10.1179/mtlr.1969.14.1.1.
18. Castro-Fernandez FR, Sellars CM, Whiteman JA. Changes of flowstress and microstructure during hot deformation of Al–1Mg–1Mn. Materials Science and Technology 1990;6;453–460. https://doi.org/10.1179/mst.1990.6.5.453.
19. Duan X, Sheppard T. Simulation and control of microstructure evolution during hot extrusion of hard aluminium alloys, Materials Science and Engineering A 2003;351(1–2);282–292. https://doi.org/10.1016/S0921-5093(02)00840-7.
20. Duan X, Sheppard T, Computation of substructural strengthening by the integration of metallurgical models into the finite element code. Computational Materials Science 2003;27;250–258. https://doi.org/10.1016/S0927-0256(02)00362-2.
21. Vatne HE, Furu T, Orsund R, Nes E. Modelling recrystallization after hot deformation of aluminum. Acta Materialia 1996;11;4463–4473. https://doi.org/10.1016/1359-6454(96)00078-X.

22. Sellars CM, Zhu Q. Microstructural modelling of aluminium alloys during thermomechanical processing. Materials Science and Engineering: A 2000;280;1-7. https://doi.org/10.1016/S0921-5093(99)00648-6.
23. Eivani AR, Zhou J, Duszczyk J, Grain boundary versus particle stimulated nucleation in hot deformed Al–4.5Zn–1Mg alloy. Materials Science and Technology 2013;29;517-528. https://doi.org/10.1179/1743284712Y.0000000176.
24. Furu T, Østhus R, Telioui N, Aagård R, Bru M, Myhr OR. Modeling the Effect of Mn on Extrudability, Mechanical Properties and Grain Structure of AA6082 Alloys. Proceedings of the Eleventh International Aluminum Extrusion Technology Seminar ET 2016, Chicago 3-6, 2016;1;567-590.
25. Peng Z, Sheppard T, Prediction of Static Recrystallisation after Extrusion of Shaped Aluminium Sections. In Materials Science Forum 2004;467–470;407–420. https://doi.org/10.4028/www.scientific.net/msf.467-470.407.
26. Güzel A, Jäger A, Parvizian F, Lambers HG, Tekkaya AE, Svendsen B, Maier HJ. A new method for determining dynamic grain structure evolution during hot aluminum extrusion. Journal of Materials Processing Technology 2012;212(1);323-330. https://doi.org/10.1016/j.jmatprotec.2011.09.018.
27. Mahmoodkhani Y, Chen J, Wells MA, Poole WJ, Parson N. The Effect of Die Bearing Geometry on Surface Recrystallization During Extrusion of an Al-Mg-Si-Mn Alloy. Metallurgical and Materials Transactions A 50 2019;5324–5335. https://doi.org/10.1007/s11661-019-05437-0
28. Eivani AR, Jafarian HR, Zhou J. Simulation of peripheral coarse grain structure during hot extrusion of AA7020 aluminum alloy. Journal of Manufacturing Processes 57 2020;881-892. https://doi.org/10.1016/j.jmapro.2020.07.011.
29. Schikorra M, Donati L, Tomesani L, Tekkaya AE. Microstructure analysis of aluminum extrusion: Prediction of microstructure on AA6060 alloy. Journal of Materials Processing Technology 2008;201(1-3);156-162. https://doi.org/10.1016/j.jmatprotec.2007.11.160.
30. Foydl A, Segatori A, Khalifa NB, Donati L, Brosius A, Tomesani L, Tekkaya AE. Grain size evolution simulation in aluminium alloys AA 6082 and AA 7020 during hot forward extrusion process. Material Science and Technology 2013;29;100–110. https://doi.org/10.1179/1743284712Y.0000000132.
31. Gamberoni A, Donati L, Reggiani B, Haase M, Tomesani L, Tekkaya AE. Industrial Benchmark 2015: Process Monitoring and Analysis of Hollow EN AW-6063 Extruded Profile. Materials Today: Proceedings 2015;2(10);4714-4725. https://doi.org/10.1016/j.matpr.2015.10.004.
32. Zhu Q, Abbod MF, Talamantes-Silva J, Sellars CM, Linkens DA, Beynon JH (2003) Hybrid modeling of aluminium-magnesium alloys during thermomechanical processing in terms of physically-based, neuro-fuzzy and finite elements models. Acta Materialia 51: 5051-5062. https://doi.org/10.1016/S1359-6454(03)00353-7.
33. Chen ZY, Xu SQ, Dong XH. Deformation behavior of AA6063 aluminium alloy after removing friction effect under hot working conditions. Acta Metallurgica Sinica (English Letters) 2008;21(6);451-458. https://doi.org/10.1016/S1006-7191(09)60008-9.
34. Humphreys FJ, Hatherly M. Recrystallization and related annealing phenomena, Second edition, Elsevier; Oxford, UK: 2004.
35. Paulsen CO. Recrystallization Behaviour in Extruded Profile of Non-Dispersoid Containing Al-Mg-Si Alloys. PhD Thesis, Department of Materials Science and Engineering NTNU-Trondheim, Materials Science and Engineering, 2015.
36. Remøe MS, Westermann I, Marthinsen K. Characterization of the Density and Spatial Distribution of Dispersoids in Al-Mg-Si Alloys. Metals 2019;9(1):26. https://doi.org/10.3390/met9010026.
37. Hensel A, Spittel T. Kraft und Arbeitsbedarf bildsamer Formgeburgsverfahren, 1. Auflage, Leipzig: VEB Deutscher Verlag fur Grundstoffindustrie 1978.
38. Negozio M, Pelaccia R, Donati L, Reggiani B, Pinter T, Tomesani L. Finite Element Model Prediction of Charge Weld Behaviour in AA6082 and AA6063 Extruded Profiles. Journal of Materials Engineering and Performance 2021;30;4691–4699. https://doi.org/10.1007/s11665-021-05752-x.
39. Gill PE, Murray W. Algorithms for the Solution of the Nonlinear Least-Squares Problem. SIAM Journal on Numerical Analysis 1978;15(5);977–992. https://doi.org/10.1137/0715063.